nature communications

Article

https://doi.org/10.1038/s41467-025-58334-z

Cryo-EM structures of a protein pore reveal a cluster of cholesterol molecules and diverse roles of membrane lipids

Received: 4 July 2024

Accepted: 17 March 2025

Published online: 26 March 2025

Check for updates

Gašper Šolinc[1], Marija Srnko[1], Franci Merzel[2], Ana Crnković[1], Mirijam Kozorog[1], Marjetka Podobnik[1] ✉ & Gregor Anderluh[1] ✉

The structure and function of membrane proteins depend on their interactions with lipids that constitute membranes. Actinoporins are α-pore-forming proteins that bind preferentially to sphingomyelin-containing membranes, where they oligomerize and form transmembrane pores. Through a comprehensive cryo-electron microscopic analysis of a pore formed by an actinoporin Fav from the coral *Orbicella faveolata*, we show that the octameric pore interacts with 112 lipids in the upper leaflet of the membrane, reveal the roles of lipids, and demonstrate that the actinoporin surface is suited for binding multiple receptor sphingomyelin molecules. When cholesterol is present in the membrane, it forms a cluster of four molecules associated with each protomer. Atomistic simulations support the structural data and reveal additional effects of the pore on the lipid membrane. These data reveal a complex network of protein-lipid and lipid-lipid interactions and an underrated role of lipids in the structure and function of transmembrane protein complexes.

Cell membranes are crucial for the functioning of organisms. A significant portion of the mammalian proteome is associated with lipid membranes[1] and many membrane-associated proteins are valuable drug targets[2]. It is becoming increasingly clear that lipids can affect proteins in many different ways, particularly in regulating the structure and function of membrane proteins[3–7]. For example, membrane lipids can also act as cofactors required for the proper functioning of membrane enzymes[8] or as structural support in the formation of membrane protein assemblies[9]. Lipids affect transporters[10,11] or ion channel gating and activity by directly interacting with the protein or indirectly by altering the properties of the membrane[12,13]. They play an important role in regulating the activity of G-protein-coupled receptors, such as serotonin receptors[14] and β2-adrenergic receptors[15], through specific binding of phospholipids or through cholesterol molecules surrounding the receptor's transmembrane domain influencing the ligand-binding pocket.

Due to the nature of protein-lipid interactions and the dynamics of lipid molecules, the determination of protein-lipid interactions at high resolution is a major challenge[16,17]. Thanks to advances in cryo-electron microscopy (cryo-EM), the number of known structures of membrane proteins with associated lipids continues to increase[17,18]. The lipids observed in these structures are usually one of two types, a single, specifically bound lipid with a well-defined density or multiple ordered acyl chains without defined headgroups in a cleft or at the interface between subunits of a larger complex[19,20]. In several cases lipids have been unambiguously identified in three dimensional structures of membrane protein complexes, providing valuable information about their effects on protein structure and function[14,21–23]. A valuable approach in the study of interactions between membrane proteins and lipids is that of molecular dynamic (MD) simulations[24]. MD simulations show that lipids close to membrane proteins diffuse slower than bulk lipids[25]. In addition, proteins and surrounding lipids form complexes whose lateral diffusion is coupled[26]. This approach has already been utilised for the study of pore-forming toxins, such as ClyA and α-HL[27,28].

Here, we used a homologue of an actinoporin pore-forming toxin fragaceatoxin C (FraC) from the coral *Orbicella faveolata*, Fav, to specifically identify and reconstruct by cryo-EM the atomic model of

[1]Department of Molecular Biology and Nanobiotechnology, National Institute of Chemistry, Ljubljana, Slovenia. [2]Theory Department, National Institute of Chemistry, Ljubljana, Slovenia. ✉e-mail: marjetka.podobnik@ki.si; gregor.anderluh@ki.si

lipid molecules associated with the transmembrane pore. The crystal structure of the octameric transmembrane pore of FraC[29] shows the positions of the headgroups of three lipids bound to a single protomer. However, how the membrane is organised around the pore and how the pore itself influences the arrangement of the membrane lipids has not yet been shown in detail. We produced stable soluble pores retaining a significant number of bound lipids, which we were able to structurally resolve and assign to different functional roles. In combination with MD simulations, we uncovered extensive lipid-protein and lipid-lipid interactions, and gained unprecedented insight into the embedding of the protein complex in the lipid membrane.

Results

Preparation of soluble Fav pores

Fav is a homologue of actinoporins with unique extensions at the N- and C-termini (Supplementary Fig. 1a). The long N-terminal extension of Fav was predicted by SWISS-MODEL[30] and AlphaFold 3[31] to be highly unstructured (Supplementary Fig. 1b). While the full-length Fav did not form crystals, we were able to crystallise and determine the crystal structure of monomeric Fav with truncated 53 N-terminal residues (ΔN53Fav). The electron density map was defined only for the residues beyond A76. The structured part of ΔN53Fav showed a clear conservation of a typical actinoporin monomer consisting of a central β-sandwich flanked by two α-helices (Supplementary Fig. 1c, d, Supplementary Table 1)[32]. The C-terminal extension (E254-M259) was completely resolved and anchored to the β-sandwich by a disulfide bond, unique among actinoporins (Supplementary Fig. 1d).

For cryo-EM analysis, Fav pores were prepared by incubating monomeric wild-type Fav with 1,2-dioleoyl-*sn*-glycero-3-phosphocholine (DOPC):sphingomyelin (SM) 1:1 (mol:mol) large unilamellar vesicles (LUVs) (Supplementary Fig. 2a). We observed pores of clearly distinguishable octameric and nonameric stoichiometries (Supplementary Fig. 2a). We tested different detergents to solubilise the pores and finally solubilized them with lauryl dimethylamine oxide. We separated the solubilized pores from excess lipids and detergents by ion-exchange chromatography and concentrated them before further use (Supplementary Fig. 2b).

The cryo-EM structure of solubilized Fav pores reveals a layer of lipids supporting the pore structure

3D cryo-EM reconstruction was successful only for octameric pores, indicating low stability of the isolated nonameric pores (Fig. 1a, Supplementary Fig. 3). The funnel-shaped transmembrane channel, built of a cluster of eight amphipathic α1-helices (residues A80-N103) that detach from the central β-sandwich cores of protomers during pore formation[33], is embedded in a micelle composed of detergents and remnant lipids. The residues upstream the N-terminal α1-helix (G1-I78) are not defined by cryo-EM density. While the overall architecture of the Fav pore determined at 2.6 Å resolution, including the cap region and the transmembrane helical cluster (Fig. 1b), is similar to that of FraC[29], there are the following notable differences. In contrast to the FraC pore, the electrostatic potential of the lumenal surface of the Fav pore in the cap region is predominantly negative (Supplementary Fig. 4a). The transmembrane channel of the Fav pore is 0.32 nm wider than that of the FraC pore, with the narrowest part of 1.54 nm in diameter located at the constriction of the channel formed by the cluster of E88 side chains (Supplementary Fig. 4a). Finally, the elongation at the C-terminus of Fav provides additional contacts between the protomers (Supplementary Fig. 4a).

Three lipid molecules per protomer with partially resolved acyl chains were previously observed in the FraC pore (Supplementary Fig. 4b, c)[29]. In the Fav pore, we clearly observed lipid densities at the corresponding positions, labelled L1-L3 (Fig. 1c, d, Supplementary Fig. 4b, c). L1 is located between two neighbouring protomers. The polar headgroup of L1 is almost completely buried between the protomers in the pore, with its phosphate group forming a hydrogen bond with the backbone amide nitrogen and carbonyl oxygen of N154 of one protomer and the backbone amide nitrogen of G243 of the neighbouring protomer (Supplementary Fig. 5). The choline headgroup of SM forms cation-π interaction with Y186[34]. The acyl chains of L1 are additionally stabilised by hydrophobic interactions with the acyl chains of L4 and L6. L2 and L3 bind to a single protomer. L2 is located below the C-terminal α2-helix and between loops 2 and 3, where its phosphate group forms a hydrogen bond with the side chain of S129 and the backbone amide of G160 and F184. Its choline group forms cation-π interactions with Y189 and Y213. L2 also interacts with lipids L5, and L1 of the neighbouring protomer. The headgroup of L3 located in the pocket below the α2-helix and the acyl chains is supported by the hydrophobic tip of the Fav loop 3 (Fig. 1d, Supplementary Fig. 5). It forms hydrogen bonds with backbone carboxyl group of F188 and side chain of Y213 and cation-π interaction with Y213. The acyl chains of L3 are stabilised by hydrophobic interactions with the protein.

In addition to L1-L3, we observed densities corresponding to three other lipids in the Fav pore, L4-L6. L4 is located near loop 2 at the interface between two protomers, and is flanked by L1 and L2. The phosphate group of L4 forms two hydrogen bonds with the side chains of T153 and T159 and cation-π interaction with F128. L5 is located at the outer edge of the pore below the α2-helix, almost completely covering L2 (Fig. 1d). Its phosphate group forms hydrogen bonds with the side chains of Y206 and Y214 from the α2-helix and also cation-π interaction with Y214 (Supplementary Fig. 5). L6 is buried between the neighbouring protomers, with its headgroup pointing towards the pore lumen through the fenestration. Its phosphate group forms a hydrogen bond with the side chain of D99, and the acyl chains are stabilised by hydrophobic interactions with adjacent transmembrane α1-helices and L1 (Fig. 1d, Supplementary Fig. 5). L1 and L6 are buried into the pore between the protomers and are therefore referred to as structural lipids (Supplementary Fig. 6). L2 and L3 are located at positions previously proposed as important for actinoporin membrane binding[29] and, together with L4 and L5 both of which positions were previously identified with co-crystallisation of monomers and 1,2-dihexanoyl-*sn*-glycero-3-phosphocholine[29], are thus referred to as receptor lipids. The headgroups of L1-L5 are well defined (Supplementary Fig. 5) and correspond to the phosphocholine headgroups of DOPC or SM used in vesicles. The densities corresponding to lipid tails can fit acyl chains of 3 (L3) to 12 carbon atoms (L1). The region under the cap of the pore contained no density (Supplementary Fig. 7a). In this void, we could observe alternative conformations of the acyl chains of L2 and L4 (Supplementary Fig. 7b, c).

Overall, the isolated wild-type pore of Fav is a protein-lipid pore complex consisting of 8 homoprotomers to which 48 lipids are stably bound. The lipid monolayer is bound to the protein by hydrogen bonds, cation-π interactions, and hydrophobic interactions, which are additionally supported by the hydrophobic interactions between the lipid tails.

Cholesterol forms ordered nanodomains under the cap of the Fav pore

The activity of actinoporins is enhanced in the presence of cholesterol[35]. Therefore, our next goal was to investigate how cholesterol affects lipid arrangement and the pore structure. Furthermore, we could not resolve which lipid is bound in the pores formed on DOPC:SM membranes, as the DOPC and SM headgroups have the same phosphocholine structure, as discussed previously[29,36]. For this reason, we used 1-palmitoyl-2-oleoyl-*sn*-glycero-3-phospho-(1'-rac-glycerol) (POPG) instead of DOPC, which has a different head group than SM and should allow differentiation of the bound lipids. We prepared wild-type Fav pores on liposomes composed of POPG:SM:cholesterol 1:1:1

https://doi.org/10.1038/s41467-025-58334-z

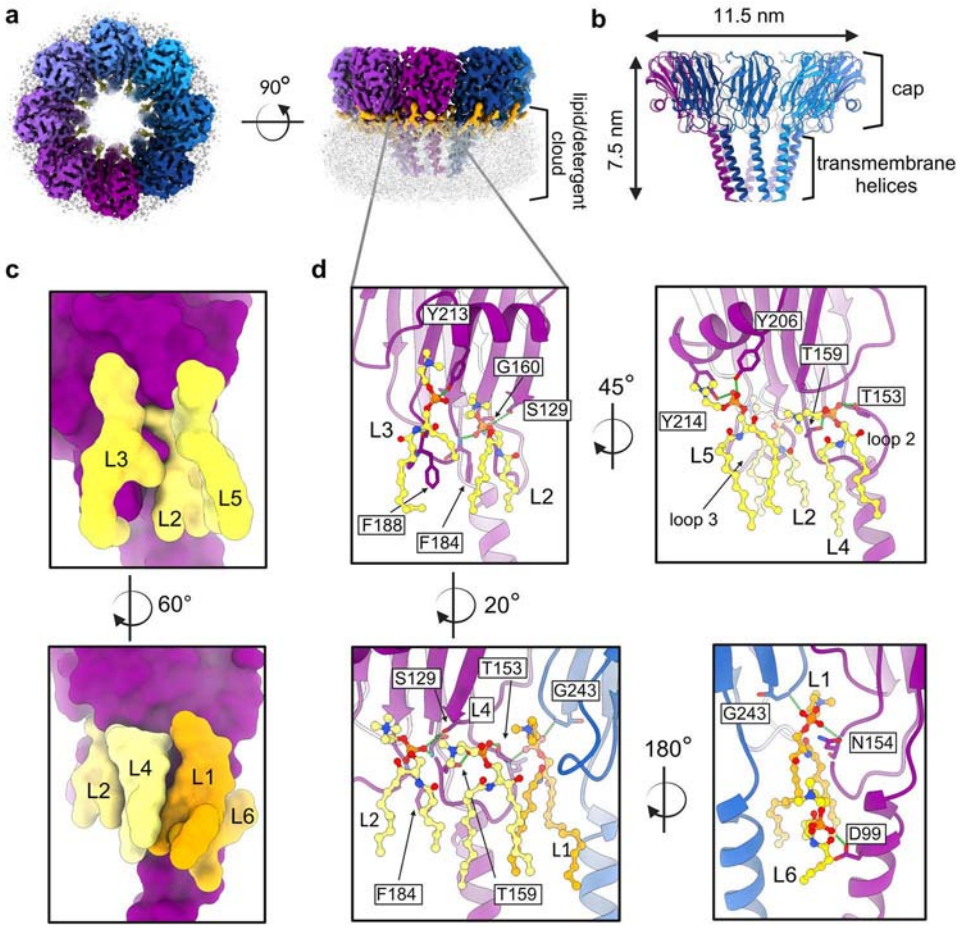

Fig. 1 | The structure of the Fav pore formed on DOPC:SM (1:1) membranes. a A top and a side view of cryo-EM map of octameric Fav pore extracted from DOPC:SM large unilamellar vesicles. Each protomer is coloured with a distinct colour, regions of the map corresponding to well-defined lipids are shown in orange. The transparent grey cloud around the bottom part of the pore is a cryo-EM density of the lipid/detergent micelle. **b** Cartoon representation of the Fav pore. The cap region and transmembrane helical cluster and pore dimensions are marked. **c** Surface representation of a single Fav pore protomer with marked six lipid positions (L1-L6; orange and yellow) identified from the pore structure (purple). **d** Detailed look at the lipid positions and their coordination. Created in BioRender. D11, O. (2025) https://BioRender.com/g24b523.

(mol:mol:mol). Cryo-EM reconstruction at 2.9 Å resolution showed a similar architecture of the pore as found in DOPC:SM membranes (Fig. 2a, Supplementary Fig. 8). However, the lipid region below the pore cap was significantly larger and better defined (Fig. 2b, Supplementary Fig. 9). We were able to resolve 15 lipids associated with each protomer, including 4 cholesterol molecules (CH1-CH4), 10 phospholipids (L1-L10) and one acyl chain (L11) per protomer (Fig. 2c).

A unique feature of the pores extracted from POPG:SM:cholesterol membranes was a patch of four cholesterol molecules (CH1-CH4) located between the transmembrane α1-helix of each protomer and the membrane binding loops 2 and 3 (Fig. 2d), and surrounded by lipids L1-L4 and L8. In all four cholesterol molecules, the hydroxyl groups point towards the bottom of the pore cap and form hydrogen bonds with the protomer (Supplementary Fig. 10). The ordered cholesterol nanodomain with a van der Waals volume of 1311 $Å^3$ fills the space under the cap of the pore, resulting in a more ordered arrangement of the acyl chains of the phospholipids bound to the pore compared to the pores from DOPC:SM membranes. Consequently, in contrast to the pores from DOPC:SM membranes, L2 and L4 adopt a single conformation.

In the presence of cholesterol, L1-L5 adopt similar positions as in the pores extracted from DOPC:SM membranes. L6 appears to be shifted up for about 8 Å along the axis of the α1-helix, which is due to a different conformation of one of the acyl chains of the neighbouring L1 acyl group in the presence of cholesterol (Supplementary Fig. 11). Moreover, we were able to build four additional phospholipids (L7-L10) per protomer and an additional acyl chain (L11) (Fig. 2c, e, Supplementary Fig. 12). L7-L9 are located between two protomers (Fig. 2e, f), however, with very limited contacts with them. L7 is located on one side of the protomer, and L8 and L9 are on the other side (Fig. 2e, f). The choline headgroup of L7 points towards the side chain of Y206 and is stabilised via cation-π interactions[34], and additionally stabilised by hydrophobic interactions with the surrounding lipids L4, L5 and L11 of the same protomer and to some extent also with L8 and L9 of the neighbouring protomer (Fig. 2e, f, Supplementary Fig. 12). The headgroup of L8 is supported by the residues of the loop 3 and its acyl chains by CH4, L3 and L9 assigned to the same protomer, and L4 and L7 from the neighbouring protomers (Supplementary Fig. 12). L9 is located in the most outer lipid shell with almost no interaction surface with the protein, and is stabilised by lipid-lipid interactions with L3, L8, and L10 assigned to the same protomer and L7 and L11 from the neighbouring protomer (Supplementary Fig. 12, Supplementary Table 2). L10 is also located in the outer shell of the lipid binding region, between L5 and L9 (Fig. 2e). L10 choline headgroup is nestled between choline headgroup of L3 and side chain of Y214 from α2-helix, and its acyl chain is stabilised by extensive interactions with the acyl chains of L3 (Supplementary Fig. 12, Supplementary Table 2). L11 could only be modelled as an acyl chain at the outer lipid shell (Fig. 2e, f),

https://doi.org/10.1038/s41467-025-58334-z

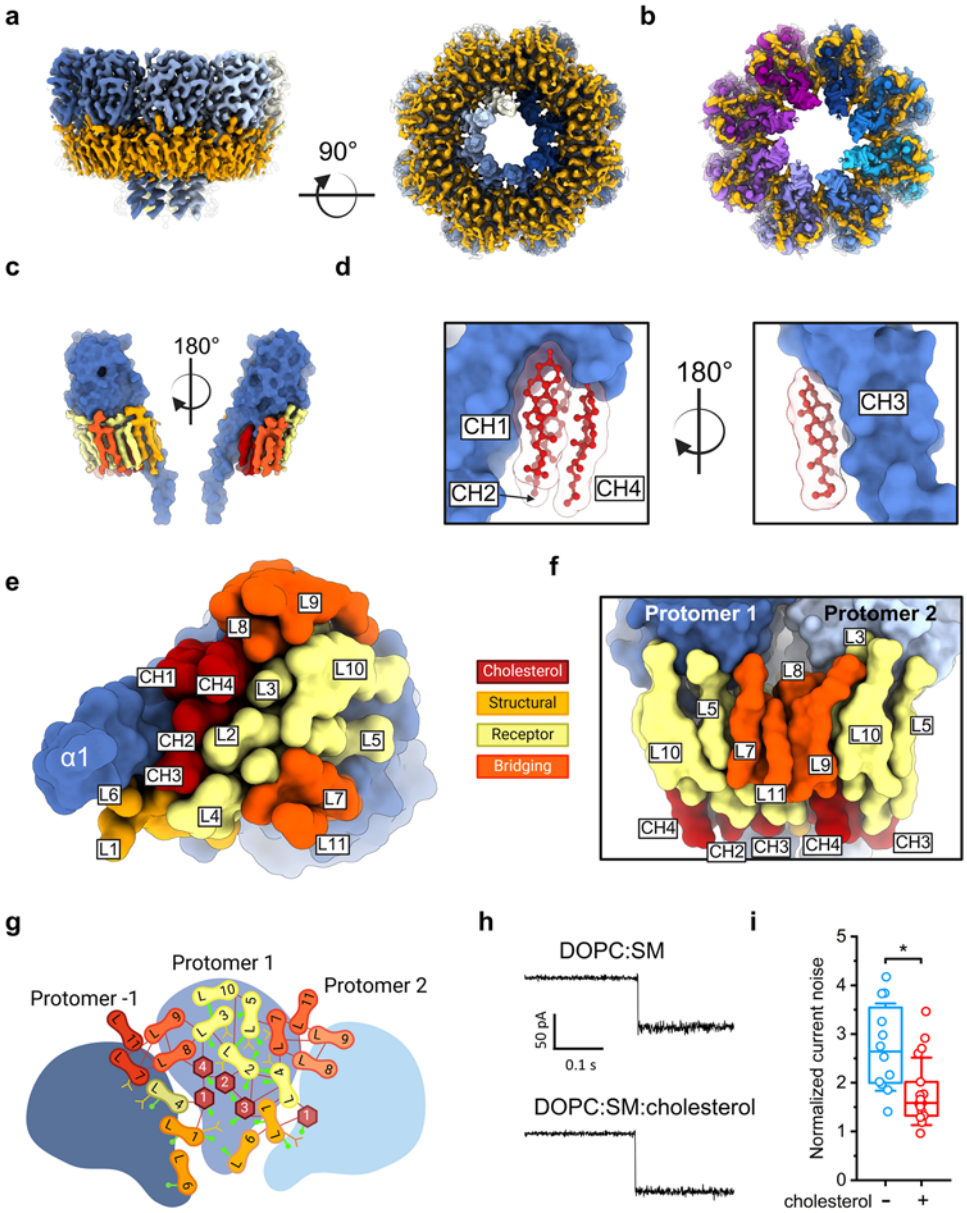

Fig. 2 | The structure of Fav pore prepared on POPG:SM:cholesterol (1:1:1) large unilamellar vesicles. a A side and bottom-up views of cryo-EM map of octameric Fav pore prepared on POPG:SM:cholesterol vesicles. **b** Bottom-up view of cryo-EM map of octameric Fav pore prepared on DOPC:SM vesicles for comparison. Parts of the map corresponding to individual pore protomers are coloured differently, and regions corresponding to well-defined lipids are shown in orange. **c** Surface representation of a Fav pore promoter with parts of the map corresponding to lipids associated with it shown at two different angles. The lipids are coloured according to the assigned function as shown in (**e**). **d** Stick and ball representation of the four cholesterol (CH) molecules in red, overlaid by the corresponding molecular surface. Pore surface is in blue. **e** A view of a Fav pore protomer in the surface presentation from the bottom of an α1-helix, showing the positions of lipids defined in the cryo-EM structure of the pore. Lipids are coloured according to the assigned function. **f** Surface representation of phospholipids resolved in the pore structure, highlighting the bridging lipids. **g** A schematic representation of lipids and proteins observed in cryo-EM structure of the Fav pore extracted from POPG:SM:cholesterol membrane. Hydrogen bonds between lipids are denoted by green lines, hydrogen bonds between lipids and proteins are denoted by a line with the circle at one end. Hydrophobic interactions between lipids are shown as red lines. Cation- π interactions between lipids and protein are indicated by orange inverted arrows. **h** Comparison of discrete ion current steps, corresponding to pore insertion induced by the addition of a monomeric Fav protein at a voltage of −50 mV in two different lipid membrane bilayers as indicated. **i** Normalised current noise for membranes from **f** in the absence (-; blue) or presence (+; red) of cholesterol. Centre line, median; box limits, upper and lower quartiles; whiskers, SD; all data points are shown. $n = 12$ and 17 single pore measurements for a membrane in the absence or presence of cholesterol, respectively. Two-sample two-sided t-test was used for statistical analysis. $^*p < 0.01$. Created in BioRender. D11, O. (2025) https://BioRender.com/g24b523.

bridging L7 of the same protomer with L8 and L9 of the neighbouring protomer (Supplementary Fig. 12). We have termed L7-L9 and L11 as bridging lipids because they have very little or no contact with the protomers. However, these lipids are in extensive contact with each other, and thus indirectly reinforce the pore structure via a protomer-1-lipid-lipid-protomer-2 bridge (Fig. 2f, g).

The presence of cholesterol in the membrane only slightly affects the position of the transmembrane helices (Supplementary Fig. 13). However, it has a small but significant effect on the ionic currents flowing through the pore. The increase in current noise upon pore formation was lower in cholesterol-containing membranes compared to cholesterol-free membranes (Fig. 2h, i).

The pores prepared with POPG:SM:cholesterol membranes, in combination with the good local resolution of the cryo-EM map, allowed us to model SM into the cryo-EM map at the positions of lipids L1-L5, thus providing structural evidence that SM can bind to positions L1-L5. The map quality of the headgroup region of L6-L11 is not high enough to distinguish between POPG and SM headgroups. In the presence of cholesterol, the acyl chains of the lipids are better defined and are now for most of the observed lipids longer than 10 carbon atoms, reaching 15 carbon atoms in L1, L2 and L5. A large part of the protomer surface is involved in membrane interaction. Of the total available 9339 Å^2 surface area of the single protomer, the amphipathic transmembrane α1-helix occupies about 2000 Å^2. Of the remaining surface area, 1500 Å^2 is involved in protomer-protomer interactions, and 2106 Å^2 in protein-lipid headgroup interactions (Supplementary Table 2). Thus, a considerable part of the protomer surface is suitable for lipid binding and is used for this purpose. Overall, we were able resolve 15 lipids associated with each protomer in the Fav pore. This monolayer patch under the pore cap is fixed by a complex network of hydrogen bonds, hydrophobic interactions and cation-π interactions. Fifteen hydrogen bonds are formed between protein and lipids and two between lipids (L2-L5 and L3-L10) (Fig. 2g).

To confirm that cholesterol and not POPG is responsible for the tighter lipid arrangement, we solved the structure of the octameric pore extracted from DOPC:SM:cholesterol 1:1:1 (mol:mol:mol) LUVs at 3.1 Å resolution (Supplementary Fig. 14a). The overall structure of the pore is almost identical with 9 phospholipids and 4 cholesterol molecules visible at comparable positions as in the pores extracted from POPG:SM:cholesterol vesicles (Supplementary Fig. 14b–e). In addition, we prepared pores on lipid nanodiscs to rule out the possibility that the observed lipid positions around the pore are an artefact of membrane solubilisation with detergents. Nanodiscs composed of DOPC:SM:cholesterol 1:1:1 (mol:mol:mol) were incubated with monomeric wild-type Fav and then analysed by cryo-EM. We were able to reconstruct the octameric pore structure with an overall resolution of 3.6 Å (Supplementary Fig. 15a). Although the quality of the cryo-EM map in this case was lower than for the solubilized pores, the cryo-EM density was present in the regions corresponding to the positions of phospholipids L1-5 and all four cholesterol molecules (Supplementary Fig. 15b), proving that the cholesterol binding positions found in the Fav pores are not an artefact of pore solubilisation.

In summary, SM binds preferentially to positions of lipids L1-L5 in the Fav pore. Moreover, the presence of cholesterol in the membranes enables compact binding of lipids to the pore and stabilisation of the pore within the membrane. This is reflected in the lower increase in ionic current noise during pore formation in cholesterol-containing membranes compared to cholesterol-free membranes (Fig. 2h, i) and in the formation of stable nonameric pores that does not dissociate during extraction from vesicles, in contrast to those formed on DOPC:SM membranes (Supplementary Figs. 3 and 8).

Loops 2 and 3 are immersed in the headgroup region of the lipid bilayer

Once the pore is formed, the amphipathic N-terminal α1-helix of each protomer spans the membrane at an angle of ~20° (Fig. 3a). During pore formation, the α1-helix is extended, from I91-V100 in the soluble monomer to A80-N103 in a transmembrane protomer of the Fav pore. The α1-helix crosses the membrane with the hydrophobic side facing the membrane along its entire length. Loops 2 and 3 are immersed in the layer of phospholipid headgroups of L1, L2, L3, L4, L6 and L8, and are lined at the bottom with the cholesterol nanodomain (Fig. 3b–d). While the overall structure of loop 3 remains virtually unchanged during the transition from the monomer in solution to the membrane-bound protomer, loop 2, residues T153-A158, moves approximately 2 Å away from the N-terminus to allow the detachment of the α1-helix from the central β-sandwich and its extension and transition through the lipid bilayer (Supplementary Fig. 16). Since the position of the two loops is independent of the presence of cholesterol, they can be described as rigid objects immersed in the headgroup region of the lipid bilayer (Fig. 3d).

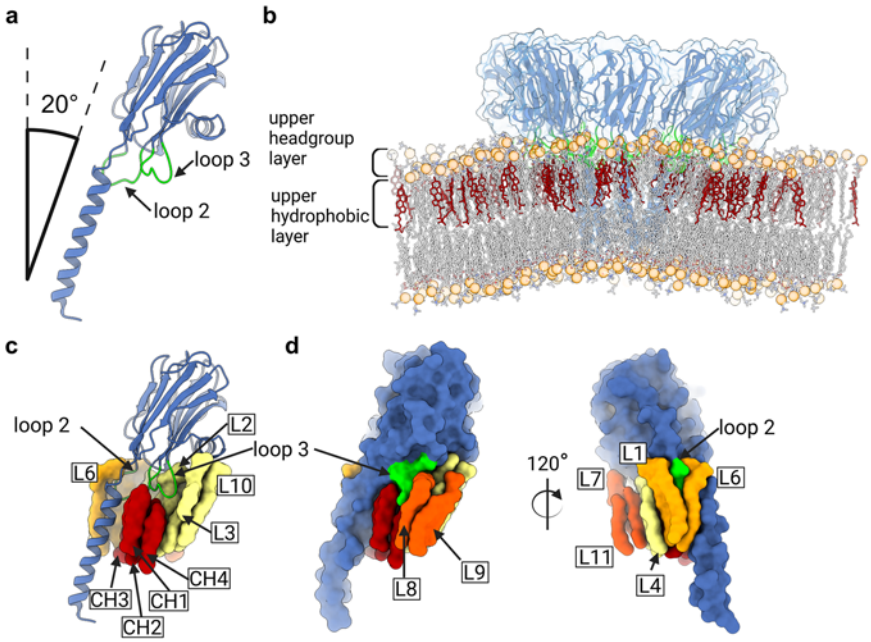

Fig. 3 | The position of the wild-type Fav pore in the membrane. a Fav protomer with membrane binding loops 2 and 3 in green. The angle at which the protomer is placed on the membrane is indicated. **b** Fav pore (blue) after minimisation embedded into a POPC:SM:cholesterol 1:1:1 (mol:mol:mol) membrane that was used for molecular modelling. Loops 2 and 3 of all protomers are shown in green cartoon, orange balls are phosphate groups of lipids and upper leaflet cholesterol molecules are shown in red sticks. **c** Cartoon representation of a protomer from the pore extracted from large unilamellar vesicles composed POPG:SM:cholesterol 1:1:1 with highlighted loops 2 and 3, with lipids surrounding it. **d** The surface representation of the Fav protomer with lipids shown at two different angles. The figure layout was created in BioRender. D11, O. (2025) https://BioRender.com/g24b523.

Sphingomyelin is essential for the oligomerization of Fav

It is known that actinoporins require SM[37,38] to effectively bind to the membrane and form pores. Our pore structures showed that lipids L1 and L6 play an important structural role. The actinoporins sticholysin II, equinatoxin II and bryoporin can bind to ceramide phosphoethanolamine (CPE), which has a smaller ethanolamine headgroup, but their permeabilization activity in CPE-containing membranes is much lower compared to SM-containing membranes[39,40]. Interestingly, we could not to obtain pores from vesicles composed of DOPC:CPE:cholesterol 1:1:1 (mol:mol:mol) (Supplementary Fig. 17), using our established method for preparation of soluble Fav pores (Supplementary Fig. 2b). Cryo-EM micrographs of multilamellar DOPC:CPE:cholesterol 1:1:1 vesicles incubated with monomeric Fav showed that the membranes were completely covered with the protein, but no pores were observed. 2D class averaging showed densely packed protein particles corresponding in size to a monomeric form of Fav bound to the membranes in multiple rows (Supplementary Fig. 17b). CPE thus enables the binding of protein to the membranes, but is not capable of triggering oligomerisation.

Due to its position in the pore structure, L1 is probably the key lipid responsible for oligomerisation, as highlighted already in Tanaka et al.[29]. The L1 head group is held in its position by formation of hydrogen bonds between its phosphate group and the side chain of R151 and the amide nitrogen of N154 of one protomer and the amide nitrogen of G243 of the adjacent protomer, and by cation-π interactions between the phosphocholine[34,41] headgroup L1 and the Y186 side chain of the neighbouring protomer (Supplementary Figs. 11 and 18). Cation-π interactions may be significantly weaker when the phosphocholine headgroup from SM is replaced by the smaller phosphoethanolamine headgroup in CPE. When CPE is placed at the position of L1, it additionally loses interactions with residue S241 (Supplementary Fig. 18b), which in the case of SM, altogether, stabilise the protomers in an oligomerised form.

The Fav pore influences the bulk membrane lipids

All-atom molecular dynamics (MD) simulations of the protein pore in a POPC:SM:cholesterol 1:1:1 (mol:mol:mol) membrane were used to verify bound lipid molecules and clarify the effect of the protein pore for the surrounding lipid molecules. During the 1.6 μs MD simulation, starting from the single pore structure with 80 SM and 32 cholesterol molecules in their predefined binding positions, not a single one of these predefined lipid molecules was detected to leave its original position (Fig. 4a, b, Supplementary Fig. 19).

To elucidate the effect of the pore-lipid interactions on structural and dynamic features of the pore surrounding lipid molecules, we focused on the correlation between displacements of lipid molecules as well as the lateral lipid diffusion as a function of the distance from the pore. We grouped SM and POPC lipid molecules into successive coordination shells around the pore in the upper and lower leaflet of the membrane as indicated in Fig. 4c. According to the evaluated correlation, the relative motion of lipid molecules is significantly more correlated in the upper leaflet as compared to the lower one (Fig. 4d). The first lipid shell (λ = 1) in both leaflets corresponds to lipid molecules in direct contact with the pore, specifically in the upper leaflet these are limited to phospholipid molecules of experimentally determined lipids involving L3, L5, L7, L8, L9 and L10. The subsequent shells

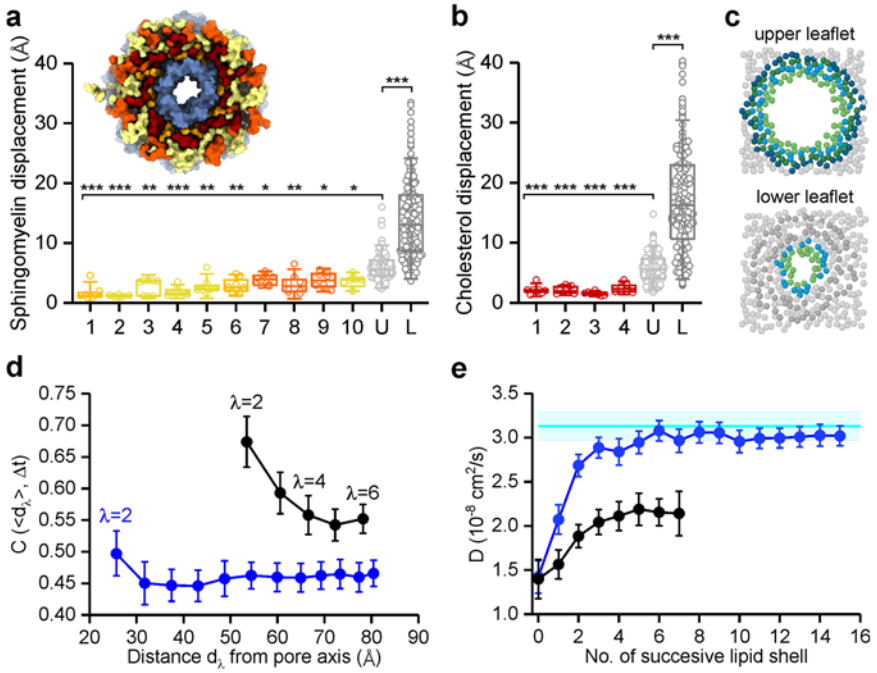

Fig. 4 | Structural and dynamic properties of membrane lipids from molecular dynamics simulations. Displacement of all predetermined sphingomyelin (1-10) (**a**) and cholesterol (1–4) (**b**) lipids as well as bulk lipids in the upper (U) and lower (L) leaflet during the 1.5 μs molecular dynamics simulation. Centre line, median; box limits, upper and lower quartiles; whiskers, SD; all data points are shown. Two-sample two-sided t-test was used for statistical analysis of displacement of lipids in the upper leaflet with all other groups of lipids. *$p < 0.01$, **$p < 0.001$, ***$p < 0.0001$. The inset in (**a**) shows the bottom view of the pore after 1.5 μs of simulation with all associated lipids labelled according to colouring scheme in Fig. 2d. **c** Schematic bead representation of SM molecules, which are divided into successive coordination shells in upper and lower membrane leaflet. Green colour represents lipids L3, L5, L7, L8, L9 and L10 in the upper leaflet. Each next successive shell is coloured blue and green, bulk lipids are grey. **d** Correlation between displacements of the neighbouring lipid molecules belonging to successive shells: current (λ) versus previous shell (λ−1) of lipids for the upper (black circles) and lower leaflet (blue circles) according to Eq. (1). Average ± SD is shown. **e** Lateral diffusion constants of the lipid molecules in successive lipid shells around the pore in the upper (black) or lower (blue) leaflet. Average ± SD is shown. The diffusion constants obtained for the pure membrane systems are given with the cyan line, together with the error range. Here, lipid shell 0 refers to diffusion constant due to the nearest protein monomer. Average and SD values in (**d**, **e**) were calculated based on analysis performed in four sequential equally long trajectory segments. The scheme in (**c**) Created in BioRender. D11, O. (2025) https://BioRender.com/g24b523.

(λ = 2, 3…) already refer to membrane lipids interacting exclusively with lipids. As a consequence of the higher correlation driven by the strong lipid-protein cap interaction, the diffusion of lipids in the upper leaflet is significantly slower compared to the lower leaflet as shown in Fig. 4e. Diffusion constants were derived from the mean square displacement (MSD) during the time up to 5 ns. However, when analysing MSDs on a longer timescale and presenting their time dependence on a log-log scale, as shown on Supplementary Fig. 20, we observe different dynamical regimes of lipid motion. Although the positive slopes of the log-log dependencies in Supplementary Fig. 20 indicate a slightly superdiffusive character of the lipid dynamics, they still clearly demonstrate the gradual slowing down of lipid mobility (diffusion) away from the pore.

Discussion

The cryo-EM structures of the Fav pores reveal general principles of protein interaction with lipids, such as details of interactions of protein with headgroups of sphingolipids and how lipids affect oligomerization, interaction with cholesterol and its effect on pore stability, how protein loops are immersed in the lipid bilayer, and together with MD simulations also highlight the concept of annular lipids that extend further than the first interactive shell of lipids.

Based on the structural and functional data, we can assign different functional roles to the lipids. The structural lipids L1 and L6 are integral part of the oligomeric pore structure. They provide an important interaction surface between the protomers and are thus an essential structural component of the pore. L1 is SM, which is essential for the oligomerization of the protein protomers into a stable octameric membrane complex, as we observed no oligomers on vesicles containing DOPC, cholesterol and CPE (Supplementary Fig. 17). One Fav protomer binds four receptor lipids, L2-L5, which can be SM molecules and for which the protein surface is very well-suited. It was shown for a homologue FraC that sites L2-L4 can be also occupied by 1,2-dihexanoyl-*sn*-glycero-3-phosphocholine, showing that both SM and PC can bind to these sites[29]. Lipid-protein interactions are stabilised by cation−π interactions between the membrane lipid headgroups and the aromatic residues of the protein and this may represent a mechanism for specific lipid recognition by membrane proteins[41]. The structures also show cholesterol nanodomains that fit very well into the gap under the cap of the Fav pore, next to the transmembrane α1-helix, and consequently stabilise the inner and outer shell of phospholipids surrounding the pore in the upper membrane leaflet. We provide structural evidence that the Fav surface can uniquely bind multiple SM headgroups, in contrast to a single lipid receptor for peripheral membrane proteins[42,43]. The cap of the Fav pore is immersed in the lipid membrane as a rigid object via the insertion of loops 2 and 3. This means that the surface of the soluble Fav monomer is already highly adapted for membrane binding, involving multiple lipids headgroups, and insertion. The advantage of binding of multiple lipid molecules is that the protein is more stably anchored to the lipid membrane. The bridging lipids have very little or no contact with the protein and can provide additional stability for pore assembly through extensive lipid-lipid interactions.

While not essential for activity, cholesterol generally enhances the pore-forming activity of actinoporins[35,44,45]. The precise mechanism behind this is unclear, but cholesterol promotes the coexistence of liquid-ordered and liquid-disordered phases, creating phase boundaries to which equinatoxin II preferentially binds[35]. It affects the compactness and fluidity, of membranes and changes the hydrogen-bonding pattern between different membrane lipids all of this can affect binding or the final formation of the pore[45–47]. Structures of Fav pores extracted from vesicles containing cholesterol and SM revealed a cluster of four cholesterol molecules per protomer. These cholesterol nanodomains are located below loops 2 and 3 next to the transmembrane α1-helix and fill the space below the pore ring. Loops 2 and 3 are immersed in the layer of lipid heads right to the depth of the membrane, where the hydrophobic layer begins, in which cholesterol molecules are located. The polar hydroxyl groups of all four cholesterols can form at least one hydrogen bond with amino acid residues in membrane-inserted loops (Supplementary Fig. 10). In addition, three cholesterol molecules from the cluster, CH1, CH2, and CH3, interact with side chains of amino acids from the transmembrane helix, while CH4 is located away from the transmembrane helix where it is stabilised mainly by neighbouring lipids (Fig. 2d, e, Supplementary Fig. 10). This interaction pattern of cholesterol molecules with the protein does not fit established protein motifs for cholesterol binding, such as CRAC[48] and CARC[49,50]. Furthermore, the pore structure in the presence or absence of cholesterol is practically the same (Supplementary Fig. 13). The presence of a cholesterol nanodomains in the pore is thus likely not due to the specific binding of cholesterol, but to the 3D structure of cholesterol nanodomain located at the right level in the membrane to fill the gap below the cap of the pore.

Most of the bound lipid molecules found in the cryo-EM pore structure exhibit low mobility in MD simulations, suggesting that the cap region of the pore almost completely restricts lipid movement below the cap. Similarly, molecular dynamics simulations showed that cholesterol molecules interact with the β-tongue region of a pore-forming toxin ClyA and dramatically slow down lipid motion near the ClyA pore[28]. The Fav pore sits on a lipid membrane patch consisting of at least 112 lipid molecules all of which stayed at their predefined position during 1.6 μs of the simulation. The pore structure also makes it possible to study the diffusion of lipids in the two lipid membrane leaflets. In the upper leaflet, the phospholipid molecules interact with the bridging lipids, while in the lower membrane leaflet the interactions take place with the cluster of transmembrane helices. The movement of lipids estimated from atomistic simulations is correlated with the movement of the pore based on the distance to it (Fig. 4d). Interestingly, the correlation of the movement between lipids falls off differently in the two leaflets in a similar manner as described before for the ClyA pore[27]. In the bottom leaflet where we observed no specific lipid binding sites on the α-helices, the lipid-lipid correlation falls off completely after lipid interaction shell 2, whereas the lipid-lipid correlation remains significant for shells 3 and even 4 in the upper leaflet. This excludes the predefined lipids observed with cryo-EM and indicates that specific protein-lipid interactions have an ordering effect that reaches further than just one additional lipid shell. As expected[25], the presence of the pore also affects the lateral diffusion constant of unbound lipids (Fig. 4e). Like in the case of the correlation between lipid movements this effect is stronger in the upper leaflet (Fig. 4d).

In summary, the structures of an actinoporin pore presented in this work illustrate the intricate interplay between the transmembrane protein and lipids and provide insights into the unique structural adaptations, ordering effects and functional consequences induced by specific lipid components. These findings contribute to a more comprehensive understanding of the behaviour of membrane proteins and lipids in membranes, highlighting the important structural and functional role of membrane lipids. In addition, we expand the pool of known pore structures with unique properties that can be used in biotechnological applications, such as in nanopore sensing[51], where the FraC pore has already been used successfully[52–54].

Methods

Protein expression and purification

Genes for all three Fav variants (wtFav, ΔN53Fav and ΔN75Fav with mutations D203R and D215N) were cloned into a modified pET28a(+) plasmid, with a His6-tag followed by TEV-cleavage site preceding the N-terminus of the target protein. Transformed *E. coli* BL21(DE3) cells were grown at 37 °C in Terrific Broth (TB), and gene expression was induced with 0.4 mM isopropyl β-D-1-thiogalactopyranoside when A_{600} reached around 0.7. After induction, the temperature was

lowered to 20 °C. Cells were harvested after 16 h by centrifugation at 6000 × *g* for 5 min at 4 °C, followed by sonication in PBS buffer pH 7.4 (1.8 mM KH_2PO_4, 140 mM NaCl, 10.1 mM Na_2HPO_4, 2.7 mM KCl). The cell lysate was centrifuged at 50,000 *g*, 4 °C for 45 min. The supernatant was filtered using a 0.22 µm syringe filter and loaded onto a NiNTA 10/50 column (Qiagen, Germany) and proteins were eluted with an increasing gradient of imidazole. The haemolytic fractions were pooled and incubated over night with addition of TEV protease with a final concentration of 1% (w/w) at 20 °C. After imidazole was removed with dialysis against PBS, the protein was again loaded onto a NiNTA 10/50 column (Qiagen, Germany) and subsequently subjected to size exclusion chromatography using Superdex 200 prep grade column (GE Healthcare, UK) equilibrated with PBS. Protein-containing factions were concentrated with Amicon Ultra Filter Devices (Millipore, USA) 10 kDa cutoff, aliquoted and stored at −70 °C.

Protein crystallisation and crystal structure determination

High-quality ΔN53Fav monomer crystals were obtained by mixing 1 µl of the protein solution with a concentration of 30 mg/ml with 1 µl of the reservoir solution containing 1.8 M Li_2SO_4 using the vapor-diffusion technique in hanging drops. The drop was equilibrated at 20 °C over 0.5 ml of reservoir solution. The rod-like crystals typically appeared within two days. Crystals were frozen in liquid nitrogen, with 20 (v/v) % 2-methyl-2,4-pentanediol as a cryoprotectant. Diffraction data was collected at 100 K and at the wavelength of 1.0 Å at XDR1 Elettra Synchrotron (Trieste, Italy). The diffraction data was processed to 1.5 Å resolution with XDS[55] (Supplementary Table 1). The crystal structure was solved using the symmetry of the space group $P3_221$ by molecular replacement (PHASER[56]), with the crystal structure of FraC (PDB-ID 3ZWJ) without loops and α-helices as a search model. Initial Δ53 Fav model was constructed with PHENIX[57] Autobuild and refined by iterative cycles of manual model building in Coot[58] and phenix.refine[59]. The crystal structure of Δ53 Fav is missing the first 25 N-terminal residues of Δ53Fav construct. There are regions of continuous electron density than likely correspond to the N-terminal region, but the density was too weak to be interpretable. The overall structure has great geometry with Molprobity score of 1.1 and the following Ramachandran parameters: favoured (98.35%), allowed (1.65%), and outliers (0.00%). The graphical presentation of the structure in the figure was done using ChimeraX v1.7[60].

Preparation of lipid vesicles

Lipid vesicles were prepared using lipids from Avanti Polar Lipids, USA. CPE, DOPC, POPG, SM, and cholesterol were dissolved in chloroform or methanol and mixed at appropriate molar ratios (1:1 or 1:1:1). Using a rotavapor (Büchi, Switzerland), a thin lipid film was created and left under a high vacuum for 2 h. The multilamellar vesicles were produced by resuspending the lipid film in PBS buffer and thoroughly vortexed with the aid of 0.5 mm glass beads (Scientific Industries, USA). The vesicles suspension then underwent at least three fast freeze/thaw cycles. Unilamellar vesicles were formed by passing the multilamellar vesicles through a LiposoFast lipid extruder (Avestin, Canada) with polycarbonate membranes with 100 nm pores.

Pore preparation

70 µM of the wild-type Fav monomer was incubated with 14 mM large unilamellar vesicles in PBS buffer for 1 h at 37 °C. The mixture was solubilized with 1 % lauryldimethylamine oxide. Sample was centrifuged for 5 min at 16,000 *g* at 20 °C to remove precipitated material. Supernatant was 20-fold diluted in buffer A (50 mM Tris, 0.25 mM Brij 35, pH 7.4) and injected to the Resource Q column (Pharmacia Biotech, Sweden) equilibrated with buffer A. Proteins were eluted with a linear gradient of buffer B (50 mM Tris, 1 M NaCl, 0.25 mM Brij 35, pH 7.4). Oligomeric state of proteins in eluted fractions was monitored with Native PAGE.

Nanodisc preparation

Plasmid pMSP1E3D1, bearing the gene for membrane scaffold protein expression was a gift from Stephen Sligar (Addgene plasmid # 20066) and was expressed as described before[61]. Shortly, *E. coli* BL21(DE3) cells transfected with the plasmid were grown in TB medium at 37 °C until A_{600} reached 2.5. Protein production was initiated with the addition of 1 mM isopropyl β-D-1-thiogalactopyranoside. Cells were harvested 3.5 h later, centrifuged at 6000 *g* and the pellet stored at − 80 °C. MSP1E3D1 protein was purified using Chelating Sepharose FF (GE Healthcare, UK) and dialyzed against MSP standard buffer (20 mM TRIS-HCl, 100 mM NaCl, 0.5 mM EDTA, pH 7.4). Protein was concentrated with Amicon Ultra-15 (Millipore, USA) to a final concentration 9 mg/ml.

The assembly of lipid nanodisc was carried out as described[62] with the following adjustments. A mixture of 5 mg DOPC, 5 mg SM and 2.5 mg cholesterol was dissolved in chloroform and methanol 1:1 (volume) mixture, and then dried in a rotary evaporator Rotavapor R215 (Buchi, Switzerland). A thin lipid film, formed in a round-bottom flask, was then hydrated by the addition of 100 µl of cholate buffer (20 mM Tris, 25 mM Na-cholate, 140 mM NaCl, pH 7.4), and vigorous vortexing and heating using warm tap water. The mixture was then sonicated in a water bath for 15 min. Finally, 250 µl of purified MSP1E3D1 were added and the mixture was incubated on a bench shaker at 4 °C for 3 h. The nanodiscs were self-assembled upon removal of Na-cholate by overnight dialysis against 3 l of PBS buffer. The dialyzed sample was purified using size-exclusion chromatography (Superdex 200 10/300, GE Healthcare Life Sciences, USA). Peak fractions, corresponding to the size of nanodiscs, were analyzed with dynamic light scattering with Prometheus Panta (Nanotemper, Germany) to confirm the presence of ~12 nm particles and the homogeneity of the solution. Concentration of nanodiscs was estimated by measuring the concentration of MSP at A_{280}. Nanodiscs were used immediately for cryo-EM experiments.

Planar lipid membranes experiments

Experiments were performed with the Orbit Mini (Nanion Technologies, Germany) set up using MECA 4 chips (Ionera, Germany). The data were collected with the Elements Data Reader v 3.8.3 (Elements, Italy) software at 20 nA working range, 20 kHz sampling frequency and room temperature. Planar lipid bilayers were prepared with the brushing method, where 10 mg/ml lipid solution in pure octane was used. To achieve pore insertion, a monomeric Fav variant (deletion of 75 amino acids from the N-terminus and D203R, D215N mutations) was applied at 1.6 µg/ml final concentration to DOPC:SM 1:1 or DOPC:SM:Cholesterol 1:1:1 membranes. For statistical analysis we calculated the mean current and its standard deviation (unfiltered current traces) for the intact membrane and the first three observed insertion steps (smaller than 200 pA). NR ratio represents the ratio between the noise of the specific insertion step (standard deviation, STD) and intact membrane noise (STD)[63]. Data were analyzed using Axon pCLAMP 11.1 (Molecular Devices, USA) software and our own MatLab R2022a (Mathworks, USA) script. Plotted traces were filtered using MatLab lowpass function with cut off frequency of 1000 Hz.

Cryo-electron microscopy sample preparation and data acquisition

Isolated wild-type Fav pores were prepared as described above (Supplementary Fig. 2b). Samples of wild-type Fav pores on vesicles were prepared similarly, excluding the solubilisation and purification steps. Instead, the sample was diluted after the incubation so that the final lipid concentration was 2 mM. Wild-type Fav pores on nanodiscs were prepared by incubating nanodiscs (0.4 mg/ml) with monomeric Fav (1 mg/mg) for 1 h at 37 °C. After incubation, the sample was 20 × concentrated with an Amicon Ultra Filter Device (Millipore, USA) (100 kDa cut-off) and 20 × diluted with PBS. This step was repeated three times to remove unbound monomers from the sample.

3 μl of each sample (purified pores, pores on vesicles and pores inserted in nanodiscs) was applied to glow-discharged (GloQube® Plus, Quorum, UK) Quantifoil R1.2/1.3 or R2/2 mesh 200 copper holey carbon grid (Quantifoil, Germany), blotted under 100% humidity at 4 °C for 6–8 s, and plunged into liquid ethane with a Mark IV Vitrobot (Thermo Fisher Scientific, USA). Micrographs of the wild-type Fav pore prepared on DOPC:SM vesicles were recorded on Titan Krios G2 (Thermo Fisher Scientific, USA) operated at 300 kV with K2 direct electron detector (Gatan, USA) at Diamond Light Source (UK), all other samples were recorded inhouse on Glacios (Thermo Fisher Scientific, USA) with a Falcon 3EC direct electron detector (Thermo Fisher Scientific, USA) and operated at 200 kV using the EPU software (Thermo Fisher Scientific, USA).

Cryo-electron microscopy data processing

All steps of data processing for all samples were performed in cryoSPARC v4[64] with built-in algorithms. Movies were aligned and dose-weighted with patch motion correction, CTF was estimated with patch CTF. Micrographs with estimated CTF fit estimation above 6 Å were excluded from further analysis. Initially, particles were picked by hand to generate 2D templates for template picking. From this point on the analysis slightly diverged for the three samples but followed similar steps. Workflows for each sample are provided (Supplementary Figs. 2, 7, 13, and 14). Particles were extracted and underwent several rounds of 2D classification. Particles from best classes were used in ab-initio reconstruction. Particles were then further cleaned up by heterogeneous refinement. Particles from the best class were then re-extracted using local motion correction and used in homogeneous refinement and non-uniform refinement with applied C8 symmetry.

Model building

Atomic models of protomers were built with the iterative use of Coot[58] and Isolde[65] plugin for ChimeraX[66]. Phenix[67] was used for applying symmetry and restraint calculation for lipid molecules. The crystal structure of ΔN53Fav monomer was used as the starting model. Details of data acquisition and refinement statistics are shown in Supplementary Table 3. The graphical presentation of the structures and cryo-EM maps in figures was done using ChimeraX v1.7[60].

Molecular dynamics simulations

All-atom models of the protein pore were prepared using the online server CHARMM-GUI[68]: the pore in a membrane composed of POPC:SM:Cholesterol 1:1:1 (mol:mol:mol) and the membrane of the same composition without the pore. The pore model was constructed from the cryo-EM structure containing 80 predefined SM and 32 cholesterol molecules by inserting it into the membrane. The pure membrane was generated to enable comparison with the bulk properties of lipid molecules. Both systems were immersed in a periodic box of lateral dimension 145 Å × 145 Å with 150 mM ionic (NaCl) concentration. Normal dimension of the simulation cell of the pore was set to 138 Å and of the pure membrane to 90 Å. Detailed MD simulation setup for both systems is presented in Supplementary Table 4. Both systems were exposed to minimisation and to a long equilibration phase of 200 ns. All simulations were carried out on GPU's with the CUDA version of the NAMD molecular dynamics[69]. The CHARMM36 force field[70] was used and water was modelled by the TIP3P water model[71]. All production simulations used the NPT ensemble and their length was at least 1.6 μs. Temperature was held constant at 303.15 K using the Langevin thermostat with a dampening constant of 1 ps^{-1}. The pressure was held constant at 1.0 bar. The cut-off for nonbonded interactions was set to 12 Å, electrostatic interactions were calculated using the Particle Mesh Ewald method (PME).

To quantify a stabilising role of the pore on lipid molecules individual lipid displacements were calculated as an average distance travelled by each lipid molecule within 1.5 μs. Correlation between displacements of molecules I and J, which are represented by centres of mass of selected atoms (beads), was evaluated through the ensemble average of displacements taking place during some chosen time Δt:

$$C_{IJ}(\Delta t)=\frac{\left\langle \left(r_I(t+\Delta t/2)-r_I(t-\Delta t/2)\right)\left(r_J(t+\Delta t/2)-r_J(t-\Delta t/2)\right)\right\rangle_t}{\sqrt{\left\langle \left(r_J(t+\Delta t/2)-r_J(t-\Delta t/2)\right)^2\right\rangle_t}\sqrt{\left\langle \left(r_I(t+\Delta t/2)-r_I(t-\Delta t/2)\right)^2\right\rangle_t}} \quad (1)$$

Displacements during the time step Δt = 5 ns were used in correlation evaluation.

Further dynamic properties of the lipid molecules were analysed by evaluating lipid lateral diffusion constant D from the time dependence of the mean-square displacements (MSD) of lipids in the membrane plane using the well-known relation[72], $<MSD(\tau)> = 4D\tau$. To ensure the characterisation of lipid diffusion per given shell around the pore, we analysed an ensemble of MSDs for all lipid molecules present in a given shell at time t, rather than focusing on the self-diffusion of a single lipid molecules. The latter migrate through different shells throughout the simulation and cannot be assigned to a single shell. The MSD of lipids in a given shell λ are calculated as $MSD_\lambda(\tau) = <[\mathbf{r}(t+\tau/2)-\mathbf{r}(t-\tau/2)]^2>$, assuming that $\mathbf{r}(t)$ pointing to the lipid molecule belongs to layer λ at time t, where <> denotes an ensemble average. The consistency of MD-derived results is shown in Supplementary Fig. 21.

Reporting summary

Further information on research design is available in the Nature Portfolio Reporting Summary linked to this article.

Data availability

All atomic coordinates have been deposited in the Protein Data Bank (PDB) under accession codes: 9EYL (monomeric ΔN53Fav), 9EYM (Fav pore extracted from DOPC:SM membrane), 9EYN (Fav pore extracted from DOPC:SM:cholesterol membrane), 9EYO (Fav pore extracted from POPG:SM:cholesterol membrane). The structure of Fav was compared to the structure of monomeric FraC 3LIM and the FraC pore structure 4TSY. The cryo-EM maps have been deposited in the Electron Microscopy Data Bank (EMDB) under accession codes: EMD-50057 (Fav pore extracted from DOPC:SM membrane), EMD-50058 (Fav pore extracted from DOPC:SM:cholesterol membrane), EMD-50059 (Fav pore extracted from POPG:SM:cholesterol membrane), EMD-50060 (Fav pore prepared on DOPC:SM:cholesterol nanodiscs). The source data underlying Figs. 2i, 4a,b, d and e, and Supplementary Figs. 2b and 17a are provided as a Source Data file. All custom codes used in this study can be obtained upon the request. Source data are provided with this paper.

References

1. Almén, M. S., Nordström, K. J. V., Fredriksson, R. & Schiöth, H. B. Mapping the human membrane proteome: a majority of the human membrane proteins can be classified according to function and evolutionary origin. *BMC Biol.* **7**, 50 (2009).
2. Overington, J. P., Al-Lazikani, B. & Hopkins, A. L. How many drug targets are there? *Nat. Rev. Drug Disc.* **5**, 993–996 (2006).
3. Levental, I. & Lyman, E. Regulation of membrane protein structure and function by their lipid nano-environment. *Nat. Rev. Mol. Cell Biol.* **24**, 107–122 (2023).
4. Lee, A. G. How lipids affect the activities of integral membrane proteins. *Biochim. Biophys. Acta.* **1666**, 62–87 (2004).
5. Barrera, N. P., Zhou, M. & Robinson, C. V. The role of lipids in defining membrane protein interactions: insights from mass spectrometry. *Trends Cell. Biol.* **23**, 1–8 (2013).
6. Corradi, V. et al. Emerging diversity in lipid-protein interactions. *Chem. Rev.* **119**, 5775–5848 (2019).
7. Han, Y. et al. Mechanical activation opens a lipid-lined pore in OSCA ion channels. *Nature* **628**, 910–918 (2024).

8. Guskov, A. et al. Cyanobacterial photosystem II at 2.9-Å resolution and the role of quinones, lipids, channels and chloride. *Nat. Struct. Mol. Biol.* **16**, 334–342 (2009).
9. Gupta, K. et al. The role of interfacial lipids in stabilizing membrane protein oligomers. *Nature* **541**, 421–424 (2017).
10. Aupič, J., Lapenta, F., Janoš, P. & Magistrato, A. Intrinsically disordered ectodomain modulates ion permeation through a metal transporter. *Proc. Natl. Acad. Sci. USA* **119**, e2214602119 (2022).
11. Martens, C. et al. Direct protein-lipid interactions shape the conformational landscape of secondary transporters. *Nat. Comm.* **9**, 4151 (2018).
12. Cordero-Morales, J. F. & Vásquez, V. How lipids contribute to ion channel function, a fat perspective on direct and indirect interactions. *Curr. Opin. Struct. Biol.* **51**, 92–98 (2018).
13. Gu, R.-X. & de Groot, B. L. Lipid-protein interactions modulate the conformational equilibrium of a potassium channel. *Nat. Comm.* **11**, 2162 (2020).
14. Xu, P. et al. Structural insights into the lipid and ligand regulation of serotonin receptors. *Nature* **592**, 469–473 (2021).
15. Dawaliby, R. et al. Allosteric regulation of G protein–coupled receptor activity by phospholipids.*Nat. Chem. Biol.* **12**, 35–39 (2016).
16. Ansell, T. B. et al. LipIDens: simulation assisted interpretation of lipid densities in cryo-EM structures of membrane proteins. *Nat. Comm.* **14**, 7774 (2023).
17. Sharma, K. D., Heberle, F. A. & Waxham, M. N. Visualizing lipid membrane structure with cryo-EM: past, present, and future. *Emerg. Top. Life Sci.* **7**, 55–65 (2023).
18. Biou, V. Lipid-membrane protein interaction visualised by cryo-EM: a review. *Biochim. Biophys. Acta.* **1865**, 184068 (2023).
19. Flores, J. A. et al. Connexin-46/50 in a dynamic lipid environment resolved by CryoEM at 1.9 Å. *Nat. Comm.* **11**, 4331 (2020).
20. Zhao, P. et al. Structure and activation mechanism of the hexameric plasma membrane H+-ATPase. *Nat. Comm.* **12**, 6439 (2021).
21. Qi, C., Di Minin, G., Vercellino, I., Wutz, A. & Korkhov, V. M. Structural basis of sterol recognition by human hedgehog receptor PTCH1. *Sci. Adv.* **5**, eaaw6490 (2019).
22. Nadezhdin, K. D. et al. Structural mechanism of heat-induced opening of a temperature-sensitive TRP channel. *Nat. Struct. Mol. Biol.* **28**, 564–572 (2021).
23. Sun, C., Zhu, H., Clark, S. & Gouaux, E. Cryo-EM structures reveal native GABA(A) receptor assemblies and pharmacology. *Nature* **622**, 195–201 (2023).
24. Chavent, M., Duncan, A. L. & Sansom, M. S. P. Molecular dynamics simulations of membrane proteins and their interactions: from nanoscale to mesoscale. *Curr. Opin. Struct. Biol.* **40**, 8–16 (2016).
25. Ebersberger, L. et al. Lipid dynamics in membranes slowed down by transmembrane proteins. *Front. Cell Dev. Biol.* **8**, 579388 (2020).
26. Niemelä, P. S. et al. Membrane proteins diffuse as dynamic complexes with lipids. *J. Am. Chem. Soc.* **132**, 7574–7575 (2010).
27. Varadarajan, V., Desikan, R. & Ayappa, K. G. Assessing the extent of the structural and dynamic modulation of membrane lipids due to pore forming toxins: insights from molecular dynamics simulations. *Soft Matter* **16**, 4840–4857 (2020).
28. Sathyanarayana, P. et al. Cholesterol promotes Cytolysin A activity by stabilizing the intermediates during pore formation. *Proc. Natl. Acad. Sci. USA* **115**, E7323–E7330 (2018).
29. Tanaka, K., Caaveiro, J. M., Morante, K., Gonzalez-Manas, J. M. & Tsumoto, K. Structural basis for self-assembly of a cytolytic pore lined by protein and lipid. *Nat. Commun.* **6**, 6337 (2015).
30. Waterhouse, A. et al. SWISS-MODEL: homology modelling of protein structures and complexes. *Nucleic Acids Res.* **46**, W296–W303 (2018).
31. Abramson, J. et al. Accurate structure prediction of biomolecular interactions with AlphaFold 3. *Nature* **630**, 493–500 (2024).
32. Athanasiadis, A., Anderluh, G., Maček, P. & Turk, D. Crystal structure of the soluble form of equinatoxin II, a pore-forming toxin from the sea anemone *Actinia equina*. *Structure* **9**, 341–346 (2001).
33. Rojko, N., Dalla Serra, M., Maček, P. & Anderluh, G. Pore formation by actinoporins, cytolysins from sea anemones. *Biochim. Biophys. Acta.* **1858**, 446–456 (2016).
34. Waheed, Q. et al. Interfacial Aromatics Mediating Cation–π Interactions with choline-containing lipids can contribute as much to peripheral protein affinity for membranes as aromatics inserted below the phosphates. *J. Phys. Chem. Lett.* **10**, 3972–3977 (2019).
35. Barlič, A. et al. Lipid phase coexistence favors membrane insertion of equinatoxin-II, a pore-forming toxin from *Actinia equina*. *J. Biol. Chem.* **279**, 34209–34216 (2004).
36. Morante, K. et al. Identification of a Membrane-bound Prepore Species Clarifies the Lytic Mechanism of Actinoporins. *J. Biol. Chem.* **291**, 19210–19219 (2016).
37. Bakrač, B. et al. Molecular determinants of sphingomyelin specificity of a eukaryotic pore-forming toxin. *J. Biol. Chem.* **283**, 18665–18677 (2008).
38. Bakrač, B. & Anderluh, G. Molecular mechanism of sphingomyelin-specific membrane binding and pore formation by actinoporins. *Adv. Exp. Med. Biol.* **677**, 106–115 (2010).
39. García-Montoya, C. et al. Sticholysin recognition of ceramide-phosphoethanolamine. *Arch. Biochem. Biophys.* **742**, 109623 (2023).
40. Šolinc, G. et al. Pore-forming moss protein bryoporin is structurally and mechanistically related to actinoporins from evolutionarily distant cnidarians. *J. Biol. Chem.* **298**, 102455 (2022).
41. Grauffel, C. et al. Cation-π interactions as lipid-specific anchors for phosphatidylinositol-specific phospholipase C. *J. Am. Chem. Soc.* **135**, 5740–5750 (2013).
42. Lemmon, M. A. Membrane recognition by phospholipid-binding domains. *Nat. Rev. Mol. Cell Biol.* **9**, 99–111 (2008).
43. Moravcevic, K., Oxley, C. L. & Lemmon, M. A. Conditional peripheral membrane proteins: facing up to limited specificity. *Structure* **20**, 15–27 (2012).
44. García-Linares, S. et al. Differential effect of membrane composition on the pore-forming ability of four different sea Anemone Actinoporins. *Biochemistry* **55**, 6630–6641 (2016).
45. Palacios-Ortega, J. et al. Sticholysin, sphingomyelin, and cholesterol: a closer look at a tripartite interaction. *Biophys. J.* **116**, 2253–2265 (2019).
46. Rojko, N. & Anderluh, G. How lipid membranes affect pore forming toxin activity. *Acc. Chem. Res.* **48**, 3073–3079 (2015).
47. Pedrera, L. et al. The presence of sterols favors sticholysin I-membrane association and pore formation regardless of their ability to form laterally segregated domains. *Langmuir* **31**, 9911–9923 (2015).
48. Li, H. & Papadopoulos, V. Peripheral-Type Benzodiazepine receptor function in cholesterol transport. identification of a putative cholesterol recognition/interaction amino acid sequence and consensus pattern. *Endocrinology* **139**, 4991–4997 (1998).
49. Baier, C. J., Fantini, J. & Barrantes, F. J. Disclosure of cholesterol recognition motifs in transmembrane domains of the human nicotinic acetylcholine receptor. *Sci. Rep.* **1**, 69 (2011).
50. Fantini, J., Epand, R. M. & Barrantes, F. J. Cholesterol-Recognition Motifs in membrane proteins. in *Direct Mechanisms in Cholesterol Modulation of Protein Function* (eds Avia R.-D. & A. N. Bukiya) 3-25 (Springer International Publishing, 2019).
51. Crnković, A., Srnko, M. & Anderluh, G. Biological nanopores: engineering on demand. *Life* **11**, 27 (2021).
52. Wloka, C., Mutter, N. L., Soskine, M., Maglia, G. & Alpha-Helical Fragaceatoxin, C. Nanopore engineered for double-stranded and single-stranded nucleic acid analysis. *Angew. Chem. Int. Ed. Engl.* **55**, 12494–12498 (2016).
53. Huang, G., Willems, K., Soskine, M., Wloka, C. & Maglia, G. Electro-osmotic capture and ionic discrimination of peptide and protein biomarkers with FraC nanopores. *Nat. Comm.* **8**, 935 (2017).

54. Huang, G., Voet, A. & Maglia, G. FraC nanopores with adjustable diameter identify the mass of opposite-charge peptides with 44 dalton resolution. *Nat. Commun.* **10**, 835 (2019).
55. Kabsch, W. Integration, scaling, space-group assignment and post-refinement. *Acta Cryst. Sect. D.* **66**, 133–144 (2010).
56. McCoy, A. J. et al. Phaser crystallographic software. *J. Appl. Cryst.* **40**, 658–674 (2007).
57. Terwilliger, T. C. et al. Iterative model building, structure refinement and density modification with the PHENIX AutoBuild wizard. *Acta Cryst. Sect. D.* **64**, 61–69 (2008).
58. Emsley, P. & Cowtan, K. Coot: model-building tools for molecular graphics. *Acta Cryst. Sect. D.* **60**, 2126–2132 (2004).
59. Afonine, P. V. et al. Towards automated crystallographic structure refinement with phenix.refine. *Acta Cryst. Sect. D.* **68**, 352–367 (2012).
60. Pettersen, E. F. et al. UCSF Chimera-a visualization system for exploratory research and analysis. *J. Comput. Chem.* **25**, 1605–1612 (2004).
61. Bayburt, T. H., Grinkova, Y. V. & Sligar, S. G. Self-assembly of discoidal phospholipid bilayer nanoparticles with membrane scaffold proteins. *Nano Lett.* **2**, 853–856 (2002).
62. Bayburt, T. H. & Sligar, S. G. Membrane protein assembly into Nanodiscs. *FEBS Lett.* **584**, 1721–1727 (2010).
63. Antonini, V. et al. Functional characterization of sticholysin I and W111C mutant reveals the sequence of the actinoporin's pore assembly. *PLoS ONE* **9**, e110824 (2014).
64. Punjani, A., Rubinstein, J. L., Fleet, D. J. & Brubaker, M. A. cryoSPARC: algorithms for rapid unsupervised cryo-EM structure determination. *Nat. Method* **14**, 290–296 (2017).
65. Croll, T. ISOLDE: a physically realistic environment for model building into low-resolution electron-density maps. *Acta Cryst. Sect. D.* **74**, 519–530 (2018).
66. Goddard, T. D. et al. UCSF ChimeraX: meeting modern challenges in visualization and analysis. *Protein Sci.* **27**, 14–25 (2018).
67. Liebschner, D. et al. Macromolecular structure determination using X-rays, neutrons and electrons: recent developments in Phenix. *Acta Cryst. Sect. D.* **75**, 861–877 (2019).
68. Lee, J. et al. CHARMM-GUI input generator for NAMD, GROMACS, AMBER, OpenMM, and CHARMM/OpenMM simulations using the CHARMM36 additive force field. *J. Chem. Theory Comput.* **12**, 405–413 (2016).
69. Phillips, J. C. et al. Scalable molecular dynamics on CPU and GPU architectures with NAMD. *J. Chem. Phys.* **153**, 044130 (2020).
70. Klauda, J. B. et al. Update of the CHARMM All-Atom additive force field for lipids: validation on six lipid types. *J. Phys. Chem.* **114**, 7830–7843 (2010).
71. Jorgensen, W. L., Chandrasekhar, J., Madura, J. D., Impey, R. W. & Klein, M. L. Comparison of simple potential functions for simulating liquid water. *J. Chem. Phys.* **79**, 926–935 (1983).
72. Zidar, J. et al. Liquid-ordered phase formation in cholesterol/sphingomyelin bilayers: all-atom molecular dynamics simulations. *J. Phys. Chem. B* **113**, 15795–15802 (2009).

Acknowledgements

This study was supported by the Slovenian Research and Innovation Agency (Program grant P1-0391 and projects J4-8225 and J4-2547) and Oxford Nanopore Technologies, UK. Structural characterisation of Fav pores was performed at the National Institute of Chemistry Cryo-EM Facility, supported by ARIS infrastructure program IO-0003. MD simulations and part of cryo-EM data analysis was performed at the Ažman Computing Center (HPC ARC) at the National Institute of Chemistry. We also thank the Centre of Excellence for Integrated Approaches in Chemistry and Biology of Proteins (CIPKeBiP), Ljubljana, for the initial crystallisation screening for ΔN53Fav monomer as well as the staff at the Elettra synchrotron, Trieste, Italy, for the valuable technical help with X-ray diffraction data collection. We acknowledge Diamond for access and support of the cryo-EM facilities at the UK national electron Bio-Imaging Centre (eBIC), proposal SW19766-2 and Jason Van Rooyen for grid preparation and data collection. The authors gratefully acknowledge the HPC RIVR consortium (www.hpc-rivr.si) and EuroHPC JU (eurohpc-ju.europa.eu) for funding this research by providing computing resources of the HPC system Vega at the Institute of Information Science (www.izum.si). Part of cryo-EM data analysis was performed at the HPC cluster Arnes (www.arnes.si). A.C. acknowledges funding from the European Union's Horizon 2020 research and innovation programme under the Marie Skłodowska-Curie grant agreement No. 896849. We thank Tomaž Švigelj for the help with protein isolations and pore preparations. We are grateful to Matic Kisovec, Toshihide Kobayashi and Alessandra Magistrato for critical reading of the manuscript.

Author contributions

Experiments were designed and conceived by G.Š., M.S., F.M., A.C., M.K., M.P., and G.A. Fav protein expression and pore preparation experiments were performed by G.Š., M.S., and A.C. Protein crystallography was performed and analysed by G.Š. and M.P. Cryo-EM structural experiments and analyses were performed by G.Š. and M.P. MSP for nanodiscs was prepared by M.K. M.S. performed planar lipid bilayer experiments and data analysis. F.M. performed MD simulations and analysed the data. M.P. and G.A. supervised the work. G.Š., M.P., and G.A. wrote the manuscript. All of the authors contributed to editing the manuscript, and support its conclusions.

Competing interests

The authors declare no competing interests.

Additional information

Supplementary information The online version contains supplementary material available at https://doi.org/10.1038/s41467-025-58334-z.

Correspondence and requests for materials should be addressed to Marjetka Podobnik or Gregor Anderluh.

Peer review information *Nature Communications* thanks the anonymous reviewers for their contribution to the peer review of this work. A peer review file is available.